Automated mapping of montane snow cover at subpixel resolution from the Landsat Thematic Mapper

Walter Rosenthal

Institute for Computational Earth System Science and Department of Geography, University of California, Santa Barbara

Jeff Dozier

School of Environmental Science and Management, University of California, Santa Barbara

Abstract. A fully automated method uses Landsat Thematic Mapper data to map snow cover in the Sierra Nevada and make quantitative estimates of the fractional snow-covered area within each pixel. We model winter and spring reference scenes as linear mixtures of image end member spectra to produce the response variables for tree-based regression and classification models. Decision trees identify cloud cover and fractional snow-covered area. We test the algorithm on a different Thematic Mapper scene and verify with high-resolution, large-format, color aerial photography. The accuracy of the automated classification of Thematic Mapper data equals that obtainable from the aerial photographs but is faster, cheaper, and covers a vastly larger area. The mapping method is insensitive to the choice of lithologic or vegetation end members, the water equivalent of the snow pack, snow grain size, or local illumination angle.

Introduction

Only a small fraction of the Earth's land area is mountainous, but montane snow packs are the major source of many regions' fresh water. For example, winter snow in the Sierra Nevada provides three quarters of California's agricultural water supply. Alpine snow and ice fields may also be sensitive indicators of the effects of climatic change on the hydrologic cycle; one possible consequence of a warmer climate is a higher snow line and a larger proportion of rain in the winter precipitation [*Gleick*, 1987].

Snow-covered area (SCA) is fundamental to the role of snow in hydrology and climate. Satellite-derived estimates of SCA are important to snowmelt runoff models [*Rango and Itten*, 1976; *Rango and Martinec*, 1979; *Martinec and Rango*, 1981] and to estimating the radiative component of the surface energy balance [*Dozier*, 1989]. Here we address two new steps in the application of remote sensing to snow mapping: (1) recognition of whether the perceived SCA within a pixel is unbroken or mixed with other surface materials and (2) quantifying the degree of mixing by determining the fraction of each pixel covered by snow.

The Landsat Thematic Mapper (TM) is suitable for estimating montane SCA because its 30-m instantaneous field-of-view (IFOV) is small compared to the scale of topographic relief in alpine regions, and its spectral bands can discriminate snow from clouds, vegetation, lithology, and open water. This study investigates three impediments to the operational use of TM data for mapping snow over rugged terrain:

1. The "mixed pixel" problem. Parts of the snow cover lie beneath a forest canopy or are interspersed with rock, soil, or vegetation. Because the recorded radiance for each pixel contains contributions from all materials within the IFOV of the

sensor, the measured spectrum is a combination of the spectra of the individual materials. The problem is severe over rugged terrain, where extreme variations in snow cover, vegetation type, canopy density, lithology, cloud cover, and atmospheric thickness occur over small horizontal distances.

2. Variable illumination. The lighting geometry typical of montane regions compounds the mixed pixel problem by producing the full range of illumination, from direct sun to shade. Snow in the shadows can be darker at all wavelengths than sunlit rock or vegetation. Diffuse sky irradiance and irradiance reflected from surrounding terrain are important sources of illumination, especially on shaded slopes. Digital elevation models (DEMs) can be used for calculating terrain view and sky view factors [*Dozier and Frew*, 1990] and for converting satellite data to hemispherical or bidirectional reflectance, but coregistration of the topographic and satellite data is difficult, and good topographic data are lacking for many of the world's mountain ranges.

3. Detector saturation. The visible bands of the TM were designed for analysis of vegetation, soils, and open water. Hence the upwelling radiance over snow and clouds often exceeds the dynamic range of the detectors [*Dozier*, 1984]. This can mask the spectral signatures of materials other than snow in a pixel.

Background

In this section we present and discuss previous work mapping snow cover from TM data, and the rationale for our approach. We have collected additional background material in the Appendix. There you will find definitions and fundamental material on the remote sensing of snow in the TM band passes, spectral mixture analysis, and decision tree methodology.

Previous Work on Mapping Snow in Mountainous Terrain from Landsat

The Landsat Multispectral Scanner System (MSS) was the predecessor to the TM. It had four bands in the visible and

near-infrared (VNIR) portion of the electromagnetic spectrum. The TM has four bands in the VNIR, at similar wavelengths to those of the MSS, two bands in the shortwave infrared (SWIR), and one band in the thermal infrared. Table A1 in the Appendix gives spectral and radiometric characteristics of the TM bands.

Rango and Itten [1976] used both supervised and unsupervised computer classification techniques to map snow-covered area in the Wind River Range from MSS data. *Martinec and Rango* [1981] used MSS data coupled with degree-day measurements from surface instruments to estimate the distribution of snow water equivalence (SWE) over an alpine basin. *Baumgartner et al.* [1985] used MSS and digital terrain data to hindcast snowmelt runoff across five elevation zones in the Swiss Alps.

Because of the commonly poor quality of digital elevation models over mountainous terrain, it usually is not feasible to accurately estimate snow-covered area by combining reflectance derived from a satellite image with pixel slope and aspect calculated from a DEM. There is significant noise in the digital elevation data that is amplified by the differencing operations in the calculation of slope and azimuth, and coregistration introduces additional errors. It is therefore possible to know the elevation of a pixel but not its illumination geometry. *Dozier and Marks* [1987] used the information in a digital elevation model to specify boundary conditions for a radiative transfer calculation, and they were thus able to map snow in a TM scene from the Sierra Nevada without requiring precise registration of the image to the terrain. They calculated top-of-atmosphere radiances from a snow surface for randomly sampled snow grain sizes and grid points from the DEM. Bispectral plots (i.e., paired combinations) of calculated radiances in TM bands fell within distinct envelopes for a range of grain sizes and contaminant amounts, and they used these to map snow in a TM scene of the same region.

Dozier [1989] demonstrated automatic snow mapping based on apparent planetary reflectance. A threshold in band 1 was used to discriminate snow from other materials in shadow, while one in band 5 distinguished snow from clouds. A normalized difference ratio of reflectance in bands 2 and 5 was used to discriminate sunlit rocks, soils, and clouds from sunlit snow.

In these approaches the classification was binary, that is, a pixel is either "snow" or "not snow." Errors result from the surface materials within a pixel not being pure snow, rock, vegetation, or water, but combinations of these.

Rosenthal [1993] used regression and classification trees referenced to a spectral mixture analysis to accurately map spring snow in the Sierra Nevada. The mixture analysis was insensitive to the choice of lithologic or vegetation spectral end members, or to topographic illumination effects.

Compensating for Topographic Effects

The surface in rugged terrain is illuminated by direct solar irradiance, diffuse sky irradiance, and both direct and diffuse irradiance reflected from surrounding terrain. All illumination on completely shaded slopes is diffuse or reflected. Surface composition (e.g., vegetation community, snow loading) often changes with slope, aspect, and elevation.

Because both rock and vegetation in the sun can be brighter at all wavelengths than snow in the shadows, simple band thresholding (or "density slicing") cannot accurately discriminate snow from other surface materials. Supervised techniques, such as parallelepiped and maximum-likelihood classifiers [*Richards*, 1993], can identify pure pixels over a wide range of illuminations if known training sites are available, but they are binary classifiers. They do not do well with spectral mixtures or deep shadows, and they require detailed knowledge of the surface because they require an adequate population of training sites. Unsupervised clustering algorithms produce myriad classes that are often based on secondary illumination and spectral mixtures and are therefore difficult to interpret.

Principal components transformations [*Richards*, 1993] and band ratioing [*Crippen*, 1988] can extract and reduce effects caused by topographic shading and can emphasize differences in surface composition. Band ratios require the reflectances of different surface materials to vary proportionally with changes in illumination, which is not the case when the TM's VNIR bands saturate over snow or cloud. Moreover, ratios involving the SWIR bands are sensitive to detector noise in deep shadows. Principal components transformations often concentrate variations in illumination in the first principal component and differences in surface composition in lower-order components, but both the orientation and the magnitude of the principal component eigenvectors are sensitive to scene composition, which changes throughout the snow season.

None of these approaches provides a means for quantifying the snow-covered area of a pixel, none addresses the problem of mixed pixels, and all lack objective standards for specifying thresholds or statistical distances that separate snow-free from snow-containing pixels.

Analysis of Spectral Mixtures

Spectral mixture analysis uses the method of least squares to model pixel spectra as linear combinations of pure component spectra (spectral "end members"; see Appendix, section A3). It can normalize for different topographic illumination if the spectra maintain characteristic shapes that differ primarily in amplitude across the full range of scene illumination. Where the spectra of shaded materials are distinct from those of sunlit materials, separate end member spectra may be used.

Classification and Regression With Tree-Based Models

We use classification and regression trees to identify regions of TM band space occupied by pixels with similar snow cover fractions or obscuring clouds. The mixture analysis can thereby be generalized to other data sets, and cloud cover and surface materials occurring outside the modeled area can be included in the analysis without violating constraints on the number of possible end members.

For operational mapping of snow cover at subpixel resolution, a decision tree is much faster than spectral unmixing because the data are classified by a small set of splitting rules rather than computation of a constrained least squares solution. A full six-band TM image of about 42 million pixels can be classified by three decision trees (to mask clouds, identify pixels containing snow, and estimate the fraction of each pixel covered by snow) in less than 10 min on a high-end, 300 MIPS workstation.

Methods

We modeled portions of winter and spring TM reference scenes of the Sierra Nevada as linear mixtures of snow, rock, and vegetation image end members. We then grew decision
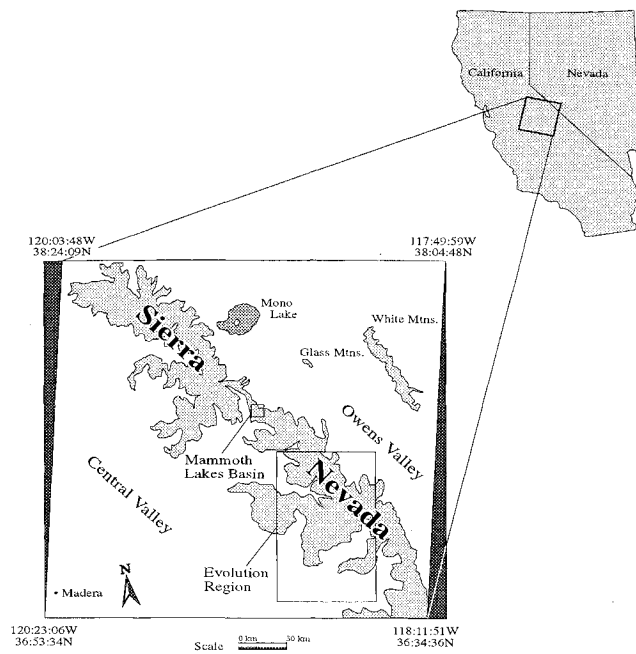
Figure 1. Map of the Sierra Nevada study area imaged in Landsat 5 Thematic Mapper (TM) path 34, row 42 (see Figure 2). The image is a swath 185 km wide by 170 km along the satellite track. Boxes indicate the location and orientation of subscenes of the Evolution region and the Mammoth Lakes Basin.

trees on a random sample of pixels from the modeled scenes, using band reflectances as the predictor variables and the corresponding scaled snow fraction from the spectral mixture analyses as the response variable. We tested the decision trees

with a new TM image, and verified our accuracy with coincident large-format, high-resolution aerial photographs. We also measured snow depth and water equivalence at field sites.
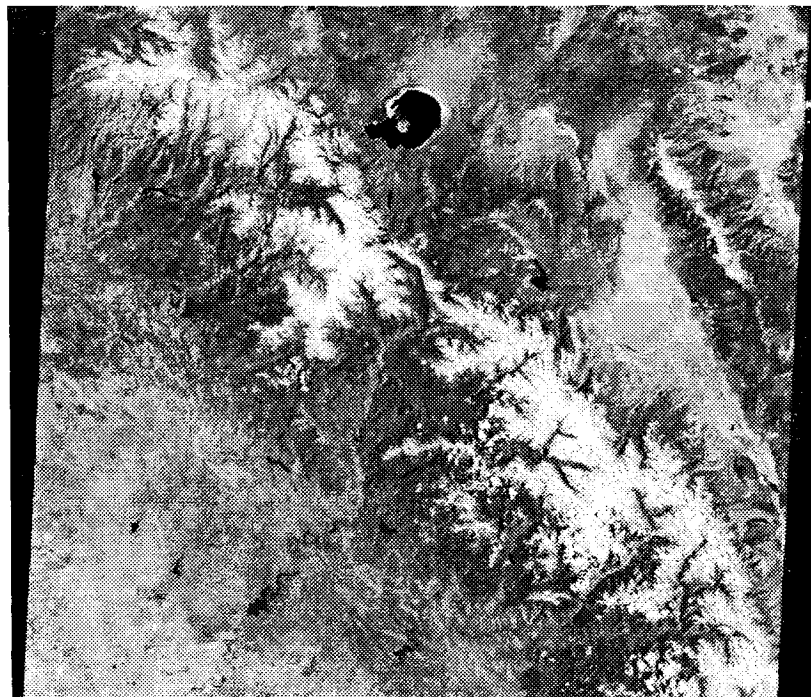
The Study Area

Figure 1 shows the study area in the Sierra Nevada. It covers a full Landsat 5 Thematic Mapper scene (path 42, row 34) and is a swath 185 km wide by 170 km along the satellite track. Elevation varies from less than 100 m in the Central Valley to over 4300 m along the crests of the Sierra Nevada and White Mountains. Mean annual precipitation across the scene increases from less than 250 mm in the Central Valley to over 1800 mm in the Sierra Nevada, then decreases to less than 150 mm in Owens Valley [*Kahrl*, 1978]. Figure 2 is a TM image of the study area.

Data Selection and Preparation

We chose the two reference scenes for spectral mixture analysis from 16 archived TM images of the study area from 1983 to 1993. Weather and snow accumulation records of the Mammoth Mountain Ski Area (near the center of the scene) were used to evaluate each scene for fresh or lingering snow on rocks or in the forest canopy.

We selected the spring reference scene, May 26, 1986, for its absence of clouds, extensive snow cover, the variety of vegetation represented, and the well-exposed, snow-free lithology. The snow depth at our 2700-m study site on Mammoth Mountain was 2.54 m, with the most recent snowfall occurring on May 7, when 0.05 m fell. This was preceded by 0.05 m of new snow on both May 4 and April 17. Air temperatures during the period were seasonally warm (e.g., the high temperature on May 26 was 19°C, and the low was 6°C). The solar zenith angle

Figure 2. Histogram-equalized TM band 4 image of the study area, TM path 34, row 42, acquired on May 10, 1992. The area is mapped in Figure 1. The swath is 185 km wide by 170 km along the satellite track. The image is skewed to compensate for the rotation of the Earth beneath the satellite as it passed from (roughly) north to south.

at the time of the satellite overpass was 32° at the scene center, and the solar azimuth was 61° east of south.

The winter reference scene, December 20, 1992, was chosen for its cloud-free area and because 0.36 m of new snow was recorded the previous morning. The total snow depth was 1.38 m, 2.36 m of snow having fallen during the preceding 2 weeks. The solar zenith angle at the time of the satellite overpass was 67°, and the solar azimuth was 29° east of south.

Atmospheric correction was limited to subtracting the additive contribution of path radiance, which we estimated by iterative ratioing for the spring scene [*Crippen*, 1987] and, because illumination extremes precluded iterative ratioing, finding the histogram minimum for the winter scene. Histogram minima for the spring scene were always within 1 or 2 digital radiance numbers (DN) of the value chosen from iterative ratioing. This type of correction relies only on information in the data, is the critical adjustment before using band ratios in the snow identification algorithm [*Crippen*, 1988], and is easy to implement in the operational automated processing of a satellite data stream. We subtracted the estimated path radiance from each band and converted the difference to apparent surface reflectance, using the calibration coefficients of *Markham and Barker* [1985, 1987].

To test the final snow-mapping algorithm, we selected a May 10, 1992, TM image because it had the least cloud cover of the 1992 spring scenes in our inventory. To compare the satellite snow classification against "truth," we obtained large-format, stereo color aerial photographs at the time of the satellite overpasses along three flight lines within the scene: Inyo Craters (elevation 2400–3170 m), Mammoth Lakes basin (2700–3370 m), and Ruby Lake basin (3370–4180 m). The camera was a nadir-viewing Wild RC-10 with an area-weighted average resolution of 83 cycles (line pairs) per millimeter. The nominal photographic scale was 1:8400 for the average surface elevation below the flight lines, resulting in a nominal ideal ground resolution of 0.1 m. The true resolution varied from this value because variations in elevation produced variations in scale along the flight lines. The photographs, which overlapped 50%, were digitized at a resolution of 12 pixels mm^{-1}, degrading the nominal resolution to about 0.7 m. The off-nadir portions were not usable for evaluating the satellite view because of (1) surface obstruction by trees and rocks, which increases away from the optical center of the photograph, and (2) "rubber sheet" distortions introduced by the rugged topography. The central portion (~10%) of each digitized photograph was registered to the TM test image.

We measured snow depth, density, grain size, and morphology along the Ruby Lake and Mammoth Lakes flight lines at the time of the satellite and aircraft overpasses. In the Mammoth Lakes basin we measured along four transects (20-m probe interval) and dug three snow pits between the elevations of 2700 and 3120 m. We measured three transects in the Ruby Lake basin between 3370 and 3700 m (100- to 200-m probe interval) with a federal sampler, which probes depth and extracts a snow core for weighing. These measurements established that even in a drought year, the Sierra snow pack could be considered optically semi-infinite (i.e., the directional-hemispherical reflectance is within 1% of that from a snow pack of infinite optical depth).

Spectral Mixture Analysis of the Reference Scenes

We conducted spectral mixture analyses on coregistered winter and spring subscenes centered on the Evolution region

of the Sierra Nevada (Figure 1). The subscene measures 47 km by 68 km (3.9 million pixels). Elevation ranges from less than 600 m to about 4300 m.

We used singular value decomposition to invert the spectral library and determine the end member fractions [*Boardman*, 1989]. The end member fractions were constrained to be nonnegative and to sum to not more than 1. By requiring the end member fractions to be physically realistic we increase our confidence in the model results. The overall RMS error will be higher for a fully constrained model than for an unconstrained one, unless the model is perfect. A low RMS error for the fully constrained model therefore indicates a good fit to the data.

End member selection. Studies using laboratory reference spectra to quantify ground cover have typically been conducted in regions of low local relief, such as the Amazon Basin or the floor of Owens Valley, California. In mountainous regions atmospheric variations and anisotropic reflectance make the use of laboratory spectra problematic. Normally one uses laboratory rather than image spectra in the end member matrix because of the assumption that homogeneous regions of pure end members are rare or nonexistent at the pixel scale. However, large areas of uninterrupted snow and monolithic rock exist within our TM scenes, and dense vegetation covers many pixels. The apparent surface reflectance spectra of rock and vegetation match the field and laboratory reference spectra gathered by *Satterwhite and Henley* [1990].

Snow: The search for snow end members was simpler than for rock or vegetation because the Sierra snow pack is composed only of nearly pure ice, air, and possibly a small amount of liquid water. However, the modeling was complicated by VNIR detector saturation and SWIR reflectance at or below the instrument noise level, and because deeply shaded snow is spectrally different from snow that is brightly illuminated. We identified bright snow end members in each scene by principal components analysis, and chose those for shaded snow iteratively from the RMS error image of the mixture analysis.

Only five bands (three VNIR and two SWIR) were used in the spring mixture model because in the spring at this latitude all image pixels containing significant amounts of snow, whether shaded or sunlit, saturate TM band 1. We modeled snow in the spring scene as a mixture of brightly illuminated (southeast facing) and shaded (northwest facing) snow (Figure 3). Both spectra are those of coarse-grained old snow. Reflectance in the SWIR bands is significant but near zero; all VNIR bands saturate for the bright snow end member, and band 3 saturates for the shaded snow end member.

Modeling the winter scene presented a different set of problems. We modeled sunlit snow by a VNIR-saturated end member and one that was unsaturated (Figure 3). Reflectances exceed unity because of anisotropic scattering by the snow. SWIR reflectance is high because the snow is new and fine grained. A third snow end member, chosen from the deeply shadowed cirque of the Darwin Glacier, was necessary for modeling shaded snow near the winter solstice. It differs from the other winter snow spectra in that SWIR reflectance is within the instrument noise level, and the VNIR reflectance is low.

Lithology: The Sierra Nevada comprises several hundred granitic plutons, large metamorphic roof pendants, and great expanses of recent volcanic rock. Numerous rock or soil end members widely distributed about the scene would mean that the decision tree learning sample would have to be drawn from many modeled subscenes of various sizes and compositions,
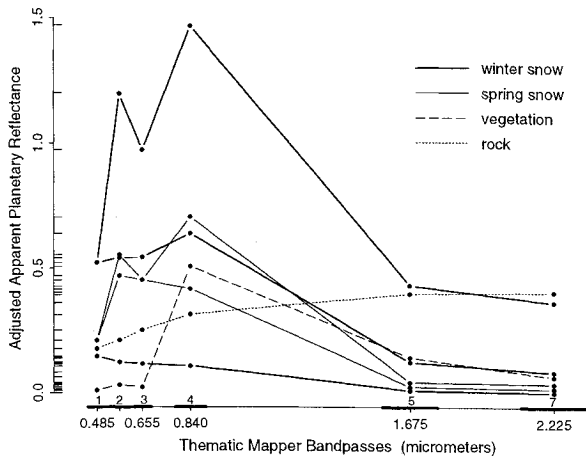
Figure 3. The final end member spectra used to model snow-covered area (SCA) over the Sierra Nevada. Rock was represented by the Half Dome granodiorite. Herbaceous vegetation from a wet meadow near Shaver Lake was the vegetation end member. The brightest winter and spring snow spectra are severely distorted by detector saturation in bands 1–4. Reflectance values can exceed unity because of extreme anisotropic reflectance from the snow pack.

greatly complicating the sampling strategy. The first task was therefore to determine the distinct lithologic end members identifiable from TM data of the Sierra Nevada and evaluate possible combinations or syntheses.

Within the study area, we identified 99 major rock units on 15 U.S. Geological Survey (USGS) geologic quadrangles (15-min series). Of these, 43 were well exposed in the May 26, 1986, reference image. We cropped a set of 18 subimages from the spring reference image for spectral mixture analysis of the influence of different rock units on estimated snow abundance.

To characterize the lithology, we ran spectral mixture analyses on the 18 subimages, minimizing the error in the 43 exposed rock units. When the brightest (Cathedral Peak granodiorite) and darkest (Ritter Range metavolcanic) spectra were mutually substituted into their respective subscene mixture models, the overall modeling errors and estimated snow abundances were insensitive to the choice of rock end member. For mapping snow, therefore, we need not distinguish between the various kinds of rock that may be exposed.

We chose Half Dome granodiorite (Figure 3) as the lithologic end member, because it is among the most extensive units in the study area and consistently produced low modeling errors in all surface classes. It outcrops throughout the Yosemite region and is similar in composition and texture to the widespread Paradise pluton of the Great Western Divide in Sequoia National Park.

Vegetation: The Sierra Nevada presents a 4000-m barrier to Pacific storms, and the resultant climatic extremes have produced a diverse assemblage of plant communities. The lithology mixture models included vegetation from the alpine zone down to about 1500 m in Owens Valley (east of the Sierra Nevada) and about 1000 m in the Central Valley (to the west). Additional subscenes were used to extend the vegetation modeling to below 400 m on the western slope south of Yosemite.

We visited the sites from which the vegetation end members were chosen after the analysis was completed. We identified vegetation to the species level except for willows, and also

noted the community type [*Storer and Usinger*, 1962; *Weeden*, 1981; *Whitney*, 1985].

The vegetation end members differed primarily in the amount of healthy, green, unshaded leaf area exposed to the sensors. This is consistent with other work suggesting that the spectral signatures of plants are not species specific but are a consequence of their composition and architecture [*Ustin et al.*, 1988; *Satterwhite and Henley*, 1990; *Smith et al.*, 1990], at least at the spectral resolution of the Landsat TM. The vegetation end member used in the final modeling was an herbaceous vegetation spectrum, chosen because it produced the lowest modeling errors in all surface classes.

Mixture model results. The reflectance $\overline{\text{RMSE}}$ (average root-mean-square error) across the winter reference scene was 0.012, or 2.7 $\overline{\text{NE}\Delta R_p}$ (mean instrument quantization steps) for all six TM bands, 1.1% of the range of the data. $\overline{\text{RMSE}}$ was 0 in deeply shaded cirques, 0 to 0.9 $\times$ $\overline{\text{NE}\Delta R_p}$ in snow-covered subalpine forests, and 0.9 to 2.7 $\times$ $\overline{\text{NE}\Delta R_p}$ in sunlit alpine basins. The highest errors occurred in patches along sunlit snow ridges, where only bands 1 and 3 would saturate, and ranged between 7 and 20. These errors were acceptable because they occurred in only a small fraction of the image pixels, and, as with the surrounding pixels, they contained only snow end member fractions.

The $\overline{\text{RMSE}}$ for the spring reference scene was also 0.012, but for that date and latitude this was 5.0 $\overline{\text{NE}\Delta R_p}$ across the scene, 2.0% of the range of the data. Errors were between 0 and 1.6 in the snow-covered subalpine forests and 3.3 to 6.5 in the thin forests at tree line and in the alpine snow fields. The $\overline{\text{RMSE}}$ over shaded snow in northwest facing cirques was 8.2. The larger error in the spring scene is attributable primarily to saturation in the VNIR bands over a large fraction of the snow pixels.

The winter and spring scaled snow fraction images were the final output of the spectral mixture modeling (Figures 4 and 5). The mean scaled snow fraction (F_{ss}, the ratio of the sum of all snow fractions to the sum of all end member fractions) for the winter model was 0.81, with 98% of the 3.91 million pixels modeled as containing snow. The mean F_{ss} for the spring model was 0.46, with 64% of the pixels modeled as containing snow. Note that in the spring scene (Figure 4), white water on the Kings River at near peak runoff is classified as snow because it is spectrally identical with snow.

We examined the influence of topography on the spectral mixture analysis by registering the scaled snow fraction models to four USGS 7.5-min digital elevation models: Blackcap Mountain, Mount Darwin, Mount Goddard, and North Palisade. We calculated the local illumination angle for each point in the DEMs, and we drew a set of 500 coordinate pairs at random for each F_{ss}/DEM pair and obtained the corresponding pixel values. Figure 6 presents the two sets of 2000 points. The spring sample mean F_{ss} is 0.79 with a mean illumination angle of 0.61 radians (~35°). The coefficient of determination $R^2 = 0.007$, and there is little or no relationship between F_{ss} and illumination angle for angles up to about 1.3 rad (~75°). The winter mean F_{ss} is 0.92, and mean illumination angle is 1.42 rad (65.4°). As in the spring data set, illumination angle has little or no influence on F_{ss} ($R^2 = 0.008$) out to at least 1.4 to 1.5 rad (80°–85° from normal).

For the 9% of the sample that is in the shade (i.e., the Sun is below the local horizon), the range of the data is restricted to values of $F_{ss} \geq 0.73$ with a mean of 0.97. Radiance near 0 (noise) in the SWIR bands could inflate F_{ss} in shaded pixels

0.0   1.0
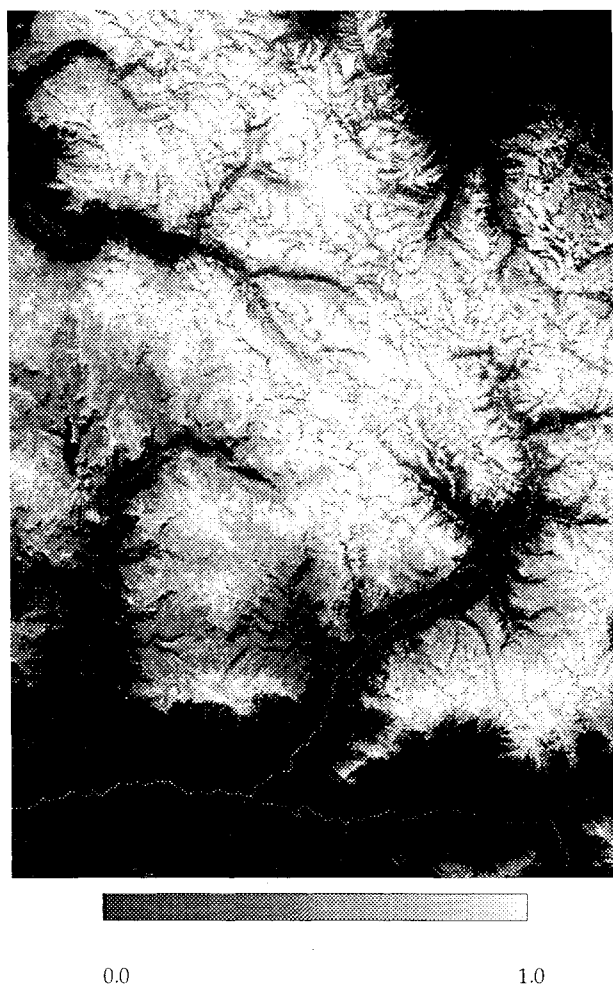
Figure 4. The May 26, 1986, Evolution region scaled snow fraction image. This is the scaled snow fraction image from which spring response variables were drawn for the decision tree learning samples. The scene dimensions are 47 by 68 km. Pixels with F_{ss} = 0 are coded black; those with F_{ss} = 1.0 are white.

where all illumination is either diffuse sky irradiance or reflected from adjacent slopes, but several factors support the model accuracy in alpine shadows. The recent snow and rime (contact-frozen, supercooled cloud droplets) would still adhere to surfaces protected from direct illumination, and shadowed cirques and canyon walls are where the deepest snow accumulation and least insolation occur. Some deeply shadowed canyons (e.g., below the confluence of the South and Middle Forks where the Kings River gorge is 1800 m deep) exhibit a full range of snow cover fractions down to 0, and visual inspection of TM bands 1 and 2 shows snow distributed throughout the shadowed regions congruent with the model results. In the absence of definitive ground or aircraft data, we tentatively accept the accuracy of the mixture model in the deepest shadows, but we continue to investigate the influence of secondary illumination on fractional snow cover estimates.

Figure 7 plots F_{ss} from the winter model against F_{ss} from the spring model for 82 subalpine forest test sites on the western slope. They lie above the spring 1986 snow line, contain a mean of 421 pixels each, and were identified in the winter false color composite image of bands 5, 4, and 2. The corresponding sites

were extracted from the models and a simple linear regression performed. Except for the two points with the largest residuals, the residuals are normally distributed and the variance is constant except at the ends of the distribution. The coefficient of determination R^2 = 0.766. If snow were distributed uniformly on the forest floor, the points should lie nearly along the 1:1 line but, even ignoring possible canopy changes from growth, fire, disease, or infestation during the 6 years between the images, this is not the case.
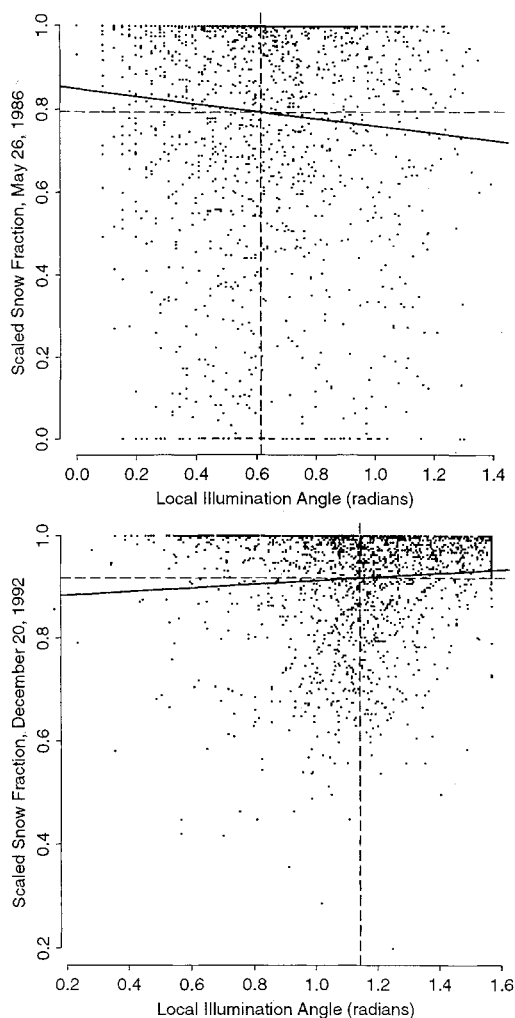
The spring data were acquired after an unusual winter with a single severe storm in February and March, followed by many weeks of warm, dry weather. Those for winter were acquired after a generally dry fall, but the day after a cold, moderately heavy storm deposited snow down to about 1000 m on both sides of the range.

Depending on depth and wetness, snow in the branches can obscure up to 100% of the canopy to nadir viewing instruments. There is, almost without doubt, snow in the canopy in the winter image, and riming is common in Sierra winter storms because of the proximity of the Pacific Ocean. Snow

0.0   1.0

Figure 5. The December 20, 1992, Evolution region scaled snow fraction image. This is the scaled snow fraction image from which winter response variables were drawn for the decision tree learning samples. The scene is coregistered with Figure 4, and the dimensions are 47 by 68 km. Pixels with F_{ss} = 0 are coded black; those with F_{ss} = 1.0 are white.

Figure 6. The relationship between illumination angle and F_{ss} for 2000 pixels. For the spring set (top), the coefficient of determination $R^2 = 0.007$, and for the winter set (bottom) $R^2 = 0.008$. The regression lines (solid) and mean values (dashed lines) are plotted. Illumination angle has little or no effect on the spectral mixture analysis.

the learning sample: 8039 cases of pixels containing snow and 1947 cases of snow-free pixels. Because it is necessary to discriminate montane snow cover from surfaces different from those found in the models, additional snow-free cases were added to the learning sample: randomly chosen pixels from the Central Valley below 500 m, from the Owens Valley floor north of Tinemaha Reservoir, and from Mono Basin (including Mono Lake, its surrounding evaporite deposits, and saline soil). The final learning sample contained 17,627 cases.

The classification tree to identify pixels containing snow was grown on the complete learning sample. The predictor variables were the apparent surface reflectances R_s in each of the six reflective TM bands, the normalized band 1 reflectance index $R_{s1}/(R_{s1} + \cdots + R_{s7})$, and the simple difference between bands 2 and 5 ($R_{s2} - R_{s5}$). The difference between bands 2 and 5 is higher for snow than for other natural substances, as is the normalized band 1 index except for bodies of water. The response variable was categorical, with a value of 0 for snow-free pixels and 1 for pixels containing snow. To assess tree stability, the sample was randomly split, and classification trees were grown on each half of the data. The trees were nearly identical in size, choice of splits, and misclassification rate. They were then discarded and a new tree grown on the full learning sample. Splitting was continued until node deviance was reduced to 0.1% that of the root node. This produced a tree of 61 terminal nodes. Tenfold cross validation showed no reduction in deviance for trees larger than 14 terminal nodes, and the large tree was pruned to 11 terminal nodes by minimum cost-complexity pruning. Tree accuracy was gauged using a 2000-pixel test sample of spring and winter data not used to grow the tree.

The regression tree for estimating SCA at subpixel resolution was grown on a learning sample restricted to those 8039 cases of pixels containing snow. The predictor variables were limited to the apparent surface reflectances R_s in each of the six reflective TM bands. No SWIR/VNIR ratios or indices were used because deep winter shadows contain only noise in the SWIR bands. The response variable was the scaled snow fraction estimated by the spectral mixture analysis. Tree stability was evaluated as above, with similar results. The final regres-

intercepted by the canopy, which thins toward the alpine tree line so that it accounts for a decreasing proportion of modeled snow cover, probably accounts for the intercept and slope of the regression line. Additional physical factors should influence the sample variance. The forest floor is not a uniform surface. Rock outcrops, shrubs, small trees, and other features are progressively covered as the snow pack thickens. In the spring the forest snow pack is littered with pine needles and branches broken by wind and snow load. Conifer trunks are then surrounded by deep wells because less snow is deposited within the drip line (snow falling through conifer branches is deflected outward and, if intercepted, also sublimates from the canopy) and because of accelerated settling, melting, and sublimation caused by thermal radiation emitted by the trunks.
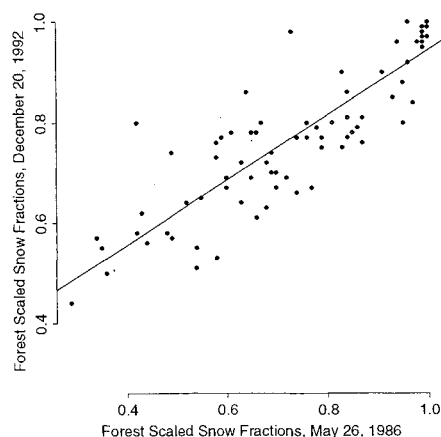
Decision Tree Analysis of the Reference Scenes

Five thousand cases each were drawn from the winter and spring Evolution TM subscenes and their respective mixture model-scaled snow fraction images. After bad data lines were eliminated from the spring set, 9986 cases were assembled into

Figure 7. December 20, 1992, scaled snow fractions versus May 26, 1986, scaled snow fractions for subalpine forest. The mean sample size was 421 pixels. The intercept is 0.296, the slope is 0.648, and the coefficient of determination R^2 is 0.766. Factors accounting for the slope of the regression line and sample variance are discussed in the text.
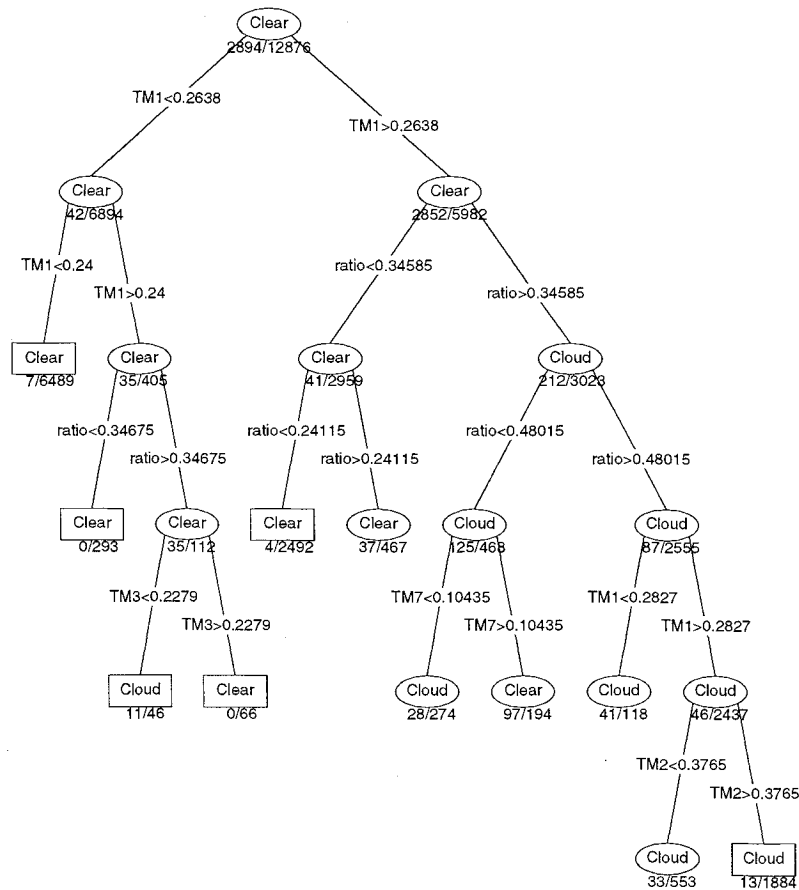
Figure 8. The core of the classification tree for detecting optically thick clouds. The full tree has 21 terminal nodes. Rectangles are terminal nodes, and ellipses are internal nodes. The fraction under each node is the ratio of misclassified cases to total cases in the node. "Ratio" is the ratio band 5/band 2. The tree misclassification rate is 0.008. Pixels identified as "cloud" are masked from further processing; those classified "clear" are passed to the snow extent classification tree.

sion tree was grown until the deviance in a node was reduced to 0.1% that of the root node, generating 109 terminal nodes. Tenfold cross validation showed that tree deviance was not reduced beyond a maximum of 40 terminal nodes, and minimum cost-complexity pruning trimmed the tree to 39 nodes. Accuracy was tested with a test sample of 2000 pixels not used to grow the tree.

Clouds were detected and masked by a classification tree. A TM scene from May 23, 1985 (path 42, row 34), containing abundant, thick cumulus clouds provided the spring cloud cases for the learning sample. The elevation of the cloud bases, estimated from shadows, surface elevation and solar geometry, was approximately 4000 m. The tops of the central updrafts were therefore much higher but could not be calculated because their shadows fell on other clouds. We obtained winter data from clouds blanketing the northwestern quadrant of the full December 20, 1992, scene. No elevation estimate was possible. To these we added random pixels from the cloud-free spring reference scene and pixels from the winter reference scene and from the Central Valley.

The combined set of 12,876 cases then constituted the learning sample for identifying clouds, with the six reflective TM bands and the ratio of band 5/band 2 as predictors, and a binary factor for the presence or absence of cloud as the

response. We used uncorrected apparent planetary reflectance R_p rather than R_s because the normally high elevation of cloud tops reduces atmospheric path radiance and increases transmittance and because an algorithm for screening clouds should not require knowledge of the atmosphere or surface beneath the clouds. Tree stability was assessed as before, with the same results. For a tree grown on the full learning sample, 10-fold cross validation showed a minimum tree deviance at 26 terminal nodes, and minimum cost-complexity pruning ultimately yielded a tree with 21 terminal nodes.

Testing the Decision Tree Model

The decision rules from all three trees (for determining cloud cover, maximum snow extent, and fractional snow-covered area, F_{SCA}) were incorporated into a program for sequentially classifying TM image data. First clouds, then surface pixels other than snow are masked, then F_{SCA} is estimated for the surviving pixels.

Coregistered regions of the digitized photographs and the 1992 TM test image were classified and compared. The mean size of TM test sites was 157 pixels, over which we averaged F_{SCA}. The mean size of the photographic test sites was 30,080 pixels, with large variation because of changes of elevation beneath the airplane.

Each photographic subimage was contrast stretched to produce a binary classification of snow cover extent, which was converted to F_{SCA} by dividing the number of snow pixels by the total pixel number.

Results

Identifying and Masking Clouds

The full cloud classification tree is too large to reproduce here, but the primary splits (reducing tree deviance 87%) are shown in Figure 8. The full tree has 21 terminal nodes, a total deviance 6.0% of that of the root node, and a misclassification rate of 0.008.

The tree reflects the physical considerations discussed in the "Background" section. Optically thick clouds have high reflectances across all TM bands. The root node split, made on R_p in band 1, reduces the tree deviance 32%. The ratio of band 5 to band 2 cleaves the right descendent node of the root into nearly pure daughter nodes, one primarily of cloud cases and the other of cloud-free. This split and the first reduce tree deviance 80%.

The misclassification rate of 0.008 is probably too low because (1) it applies only to optically thick clouds, not to thin clouds through which the ground is visible, and (2) land surfaces that, like clouds, are reflective across the solar spectrum (e.g., evaporite deposits and white water in steep mountain canyons) may be misclassified as cloud. Snow mapping through thin clouds is not addressed further in this paper, but errors of the second type are acceptable because such surfaces are not snow and should be masked.

Estimating Maximum Snow Extent

The classification tree shown in Figure 9 identifies pixels containing snow. The tree provides a parsimonious description of the data; there are only 11 terminal nodes, and the first split reduces the total tree deviance 81.2%. The difference in reflectance between TM bands 2 and 5 will always be positive or only slightly negative for pixels containing snow. The left branch off the root is then classified with the normalized band 1 index only because, except for open water (where most reflectance is in band 1), this value is higher for snow than for other surfaces. After the third level of splits only a single node (containing 1.7% of the cases) is not terminal. The final tree deviance is 7.1% that of the root node, and the misclassification rate is 0.012. The misclassification rate on the 2000-case test sample, a better indicator of predictive skill, is 0.052.

Estimating Fractional SCA

The regression tree for estimating SCA at subpixel resolution has 39 terminal nodes, a total deviance 9.63% of that of the root node, and a standard error of 0.073. The test sample standard error is 0.105. The full tree is too large to reproduce here, but the primary splits are shown in Figure 10.

The splits reflect the considerations discussed in the "Background" section. Within a given node a split on a visible TM band will assign pixels with higher reflectances to higher snow cover fractions, and those with lower reflectances to lower fractions. Conversely, splits on SWIR reflectance send brighter pixels to the daughter node containing lower snow cover fractions.

Including the ratio between bands 5 and 2 in the learning sample produces a regression tree with only 10 terminal nodes and a total deviance less than that of the tree shown here.
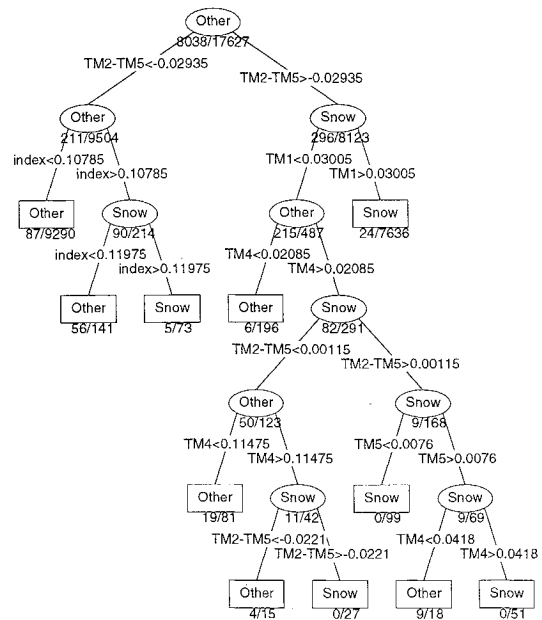
Figure 9. The maximum snow extent classification tree used to mask water and other surface types that cannot be snow. "Index" is the normalized band 1 reflectance. The tree misclassification rate is 0.012, and the test sample misclassification rate is 0.052. Pixels classified as "other" are masked from further processing; those classified as "snow" are passed to the regression tree for estimating fractional SCA.

Ratios efficiently partition the band space with planes through the origin that must be approximated by step functions of single bands. The price of such parsimony is accuracy, for all deeply shadowed pixels, regardless of snow content, are classified as pure snow.

Evaluating the Decision Tree Algorithm

Figure 11 is the classified May 12, 1992, test image produced by the decision tree program. Almost all clouds detectable in false color composite images are masked. Snow is mapped in the Sierra Nevada, Glass Mountains, and White Mountains. The only visually detectable errors occur (1) at several point locations on the floor of the Central and Owens Valleys and in the desert northeast of the White Mountains; and (2) in two of the dozens of large bodies of water in the scene: Mono and Bass Lakes. These errors are detailed in the "Discussion" section.

Because Figure 11 is printed at low resolution, the Mammoth Lakes basin portion of the classified test image is shown in Figure 12. One of the three aerial photo flight lines extended from Mammoth Mountain, at the upper left, to Duck Lake at the lower right.

Regression tree estimates of F_{SCA} for 46 regions in the TM test scene, and those obtained from corresponding regions in the large format aerial photographs are plotted in Figure 13. The relationship is linear and well modeled by a simple linear regression with an intercept of -0.009 and a slope of 0.978. The coefficient of determination $R^2 = 0.979$, and the standard deviation of the F_{SCA} estimate is 0.043. A normal probability plot shows the residuals to be normally distributed, while a plot of the standardized residuals versus predicted aerial photo values shows constant variance across the range of
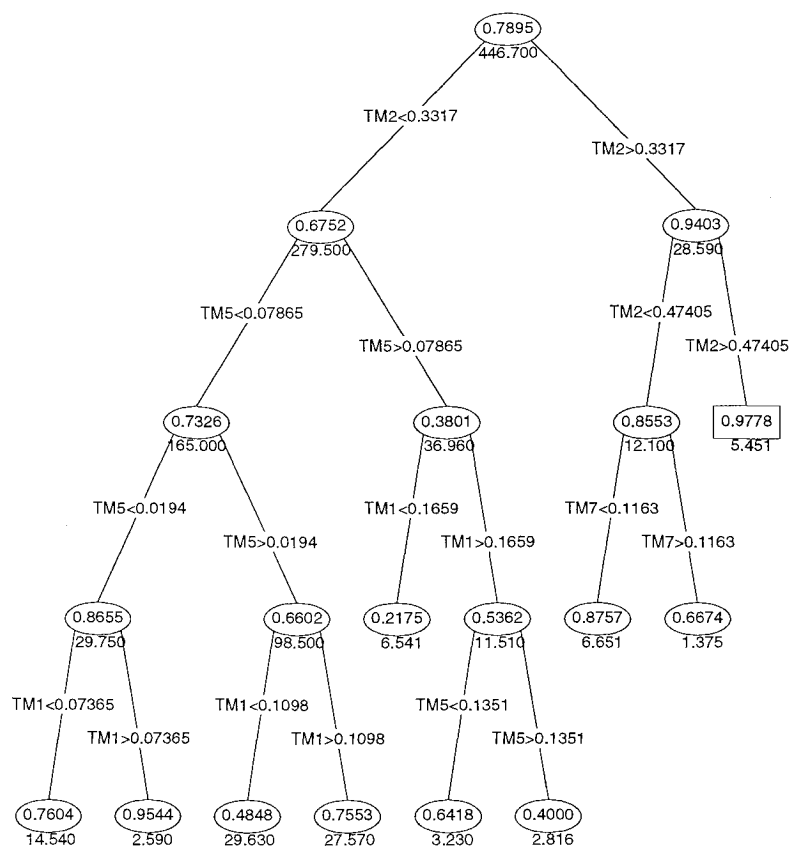
Figure 10.   The core of the fractional SCA regression tree. The mean F_{SCA} is within each node, and the node deviance is beneath. Only one node is terminal. The full tree has 39 terminal nodes and a standard error of 0.073. The test sample standard error is 0.105.

the data. Making the assumption that the errors are normally and independently distributed, and using student's t statistic for 44° of freedom, the 95% confidence interval for the slope is from 0.934 to 1.02, and for the intercept is from -0.039 to $+0.022$. The hypotheses that the regression line has a slope of 1 and an intercept of 0 for the distribution $(t_{0.025,44})$ cannot be rejected.

Discussion

Failure to reject the hypothesis suggests that the accuracy of the automated classification using TM data equals that obtainable from high-resolution aerial photography, while being faster, cheaper, and covering a vastly larger area.

In the introduction we identified three factors that hamper operational snow mapping from TM data: mixed pixels, variable illumination, and detector saturation. Our results show considerable progress toward removing these obstacles. The strength of the relationship between photographic and TM estimates of snow-covered area suggests that we can accurately measure SCA at subpixel resolution either directly, by mixture modeling, or indirectly, by regression trees referenced to modeled scenes. Figure 6 offers strong evidence that we have made substantial progress in dealing with illumination effects. Figure 13 provides evidence that detector saturation does not pose a significant problem to the mixture and tree-based models. The May 10 test image suffers from severe band saturation prob-

lems, yet the variance remains constant for the highest F_{SCA} estimates.

Because the learning sample cases span a large range of snow grain sizes and illumination conditions, the decision trees should provide accurate estimates of snow-covered area at subpixel resolution throughout the year in the Sierra Nevada and in montane regions with similar lithologies, vegetation communities, and ranges of illumination. We have classified other Sierra Nevada TM scenes from midwinter to late summer; our results agree with visual observations, but there is no supporting aerial photography.

Individual mixture models are sensitive to snow grain size, so a wide range of snow types must be modeled to generate the learning sample for the decision trees. The approach's insensitivity to grain size is a result of regression tree decision boundaries that segregate regions of TM band space occupied by pixels with similar snow cover fractions. As additional snow types and illumination geometries are added to our learning sample, we expect these regions to become more continuous and the trees to become even more robust. The variations in reflectance between different rock or vegetation types are much greater than variation between snow of different grain sizes. We have tested the influence of different rock and vegetation types on the accuracy of snow mapping and found them to be small.

The trees developed here are noteworthy because they demonstrate the power of such classifiers, but they should be

0.0   0.98
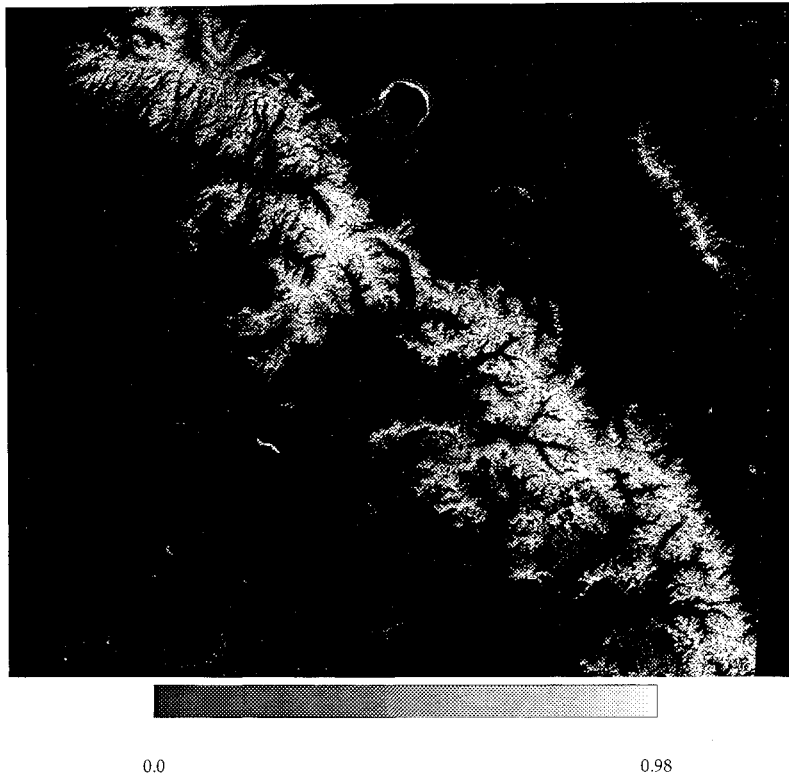
Figure 11. Fractional snow covered area, F_{SCA}, over the Sierra Nevada, Glass Mountains, and White Mountains on May 10, 1992, estimated by the regression tree in Figure 10. This is the same area mapped in Figure 1, and should be compared with Figure 2. The crescent of "snow" around Mono Lake is submerged lake bottom. Bass Lake is the bright, elongated patch a third of the way in from the left and up from the bottom. These mapping errors are discussed in the text.

0.0   0.98
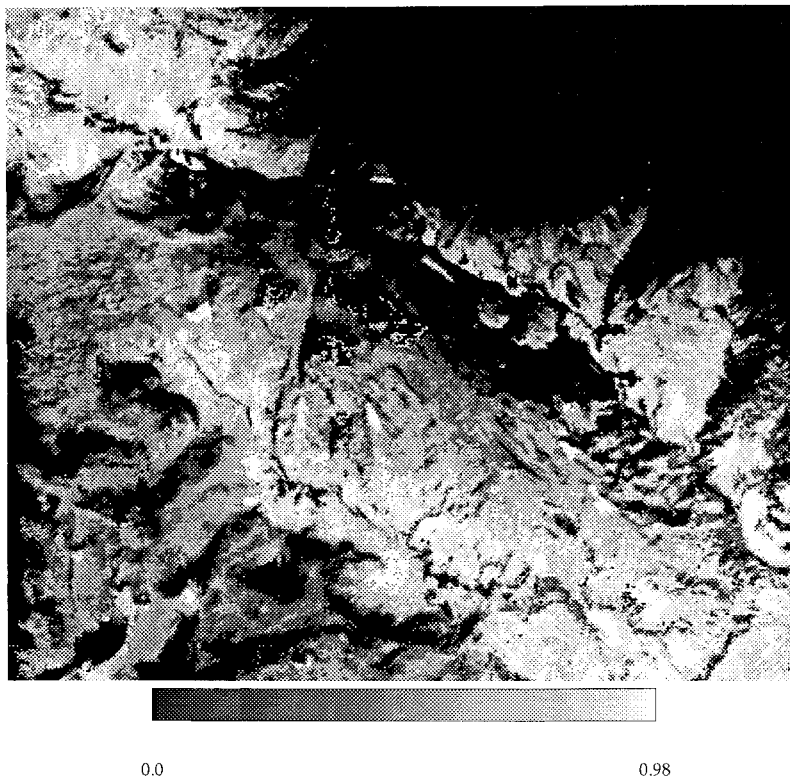
Figure 12. Image of F_{SCA} over the Mammoth Lakes basin. The scene is located in Figure 1 and measures about 11 by 9 km. One of the three photographic flight lines for testing the decision tree algorithm was from Mammoth Mountain (upper left) to Duck Lake (lower right). Much rock and vegetation is exposed because the 1992 water year was unusually dry. Probed snow depth in the basin on May 10 did not exceed 1 m.
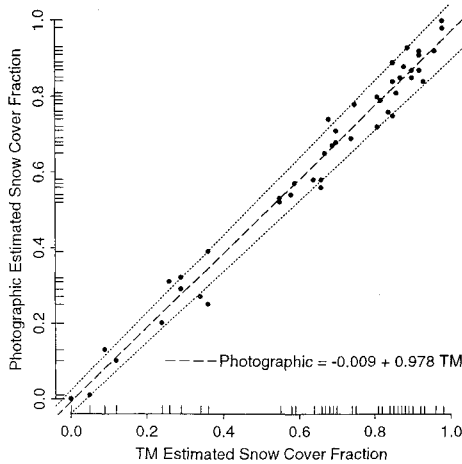
Figure 13. Photographic versus Thematic Mapper and regression tree estimates of F_{SCA} for 46 test sites. The mean size of the TM test sites was 157 pixels, and of the photographic test sites, 30,080 pixels. The coefficient of determination is 0.979. The 95% confidence intervals for the intercept and slope are plotted (dotted lines). The hypotheses that the regression line has a slope of 1 and an intercept of 0 for the distribution ($t_{0.025,44}$), and that the accuracies of the methods are therefore equivalent, cannot be rejected.

viewed as beginning rather than end products of the research. In our current work their role is being extended to the start of the modeling process, so that the spectral mixture analysis can be automated. We use decision trees to screen pixels containing snow from those that do not. Then we model the pixel sets separately with different sets of end members. The mixture model provides additional cases to modify the decision trees in an ever evolving classification system.

Mechanisms that enhance VNIR reflectance or depress SWIR reflectance may lead to the false identification of snow. Examples include water beneath a turbid atmosphere, thin clouds or fog; frozen lake surfaces and glacier ice; wet desert playas or saline soils; white river water; and dark water mixed with bright shore.

The May 10 classified image illustrates this. The bright crescent of "snow" around Mono Lake is entirely underwater and is sandy lake bottom up to 1 km offshore. The topographic gradient in this area is about 0.005. The region mapped as snow is less than 5 m deep, usually less than 1 or 2 m. The water-covered sand is spectrally similar to snow and is as bright as snow in the shadows. Bass Lake is mapped as 85% snow covered but, at approximately 1000 m elevation, is well below the snow line. All other large reservoirs on the west slope, at both lower and higher elevations (and therefore probably under both more and less turbid atmospheres) are classified as snow-free and masked. This error may be caused by shallow lake depth, suspended sediment or phytoplankton, or an oil film from boat engines.

These examples suggest that an operational subresolution snow mapping scheme will have to incorporate a choice between two types of errors. We can accept the current classification errors, perhaps using auxiliary information to mask them, or the decision trees can be pruned to eliminate some of the errors at the cost of masking some snow, primarily during winter in the forests.

Our results suggest that the spectral unmixing and decision tree methods can be extended to wide-swath sensors with better temporal but poorer spatial resolution such as the current National Oceanic and Atmospheric Administration's advanced very high resolution radiometer (NOAA/AVHRR) and the future EOS moderate-resolution imaging spectrometer (EOS/MODIS) [*Running et al.*, 1994]. MODIS will not saturate over snow, and its 20 spectral bands between 0.4 and 3.0 μm will permit the use of more end members. MODIS mixture models will also be more overdetermined, leading to greater confidence in the SCA estimates.

Conclusions

We have presented a decision tree algorithm for automated snow mapping over mountainous terrain using Landsat Thematic Mapper data. Classification trees mask cloud cover and other targets distinct from snow, and a regression tree estimates fractional SCA at subpixel resolution. We derived the algorithm from spectral mixture analyses of winter and spring reference scenes from the Sierra Nevada.

Our results suggest that snow fraction estimates from the satellite data can be as accurate as those attainable with high-resolution aerial photography, but they are obtained faster, at much lower cost, and over a vastly larger area. The algorithm is insensitive to the choice of rock or vegetation end members or to snow pack physical parameters such as the size of the snow grains, the snow-water equivalent of the pack, or the levels of particulate contamination common to maritime ranges like the Sierra Nevada. Variable illumination caused by topography has little or no apparent effect on estimated snow abundance.

The long-range benefits from this work extend beyond rapid snow mapping with TM data on a 16 day repeat period. TM data may be used as reference data for wide-swath sensors with better temporal but poorer spatial resolution such as the current NOAA/AVHRR and the future EOS/MODIS. Parallel algorithms developed for these instruments should permit the routine daily snow mapping necessary to take advantage of the infrequent clear weather over many of the Earth's mountain ranges during the precipitation and run-off seasons.

Appendix

A.1. Definitions

Radiative transfer in snow can be modeled as a multiple scattering problem in which Mie calculations provide the scattering properties of "optically equivalent spheres," perhaps having the same surface to volume ratios as the irregularly shaped ice grains [*Wiscombe and Warren*, 1980]. Parameters calculated from the Mie equations are used in radiative transfer calculations to solve for R, the spectral directional-hemispherical reflectance of the snow pack [*Meador and Weaver*, 1980; *Dozier*, 1989]. R, also called spectral albedo, is the ratio of the angular integration of the upwelling radiance (intensity) to the incoming direct irradiance (flux density):

$$R(\mu_0) = \frac{\int_0^{2\pi} \int_0^1 \mu L(\mu, \phi) \, d\mu \, d\phi}{\mu_0 F_0} = \frac{F_\uparrow}{\mu_0 F_0} \qquad (1)$$

F_0 is the direct spectral irradiance on a surface normal to the beam, μ_0 is the cosine of the solar illumination angle (mea-

Table A1. Landsat 5 Thematic Mapper Band Characteristics

Band	Wavelength Interval, μm	Spectral Region	Saturation Radiance, Wm^{-2} μm^{-1} sr^{-1}	Saturation Reflectance		
				May 26, 1986	Dec. 20, 1992	May 10, 1992
1	0.45–0.52	Visible	152.1	0.2916	0.6037	0.2962
2	0.53–0.61	Visible	296.8	0.6085	1.2605	0.6182
3	0.62–0.69	Visible	204.3	0.4874	1.0192	0.4952
4	0.78–0.90	NIR	206.2	0.7316	1.5298	0.7432
5	1.57–1.78	SWIR	27.19	0.4668	0.9631	0.4743
7	2.10–2.35	SWIR	14.38	0.7243	1.4989	0.7358

The Landsat 5 Thematic Mapper band passes for reflected solar irradiance range from the visible to the near infrared (NIR) and the shortwave infrared (SWIR). The instrument IFOV is 30 m for the reflective bands, but pixels are resampled to 28.5 m because of instantaneous field-of-view (IFOV) overlap. The radiances are recorded as 8-bit digital radiance numbers (DN) from 0 to 255. Saturation radiances correspond to DN = 255. The corresponding saturation reflectances are apparent planetary reflectances for the center of the Sierra Nevada study area, calculated for the solar angle and Earth-Sun distance on the given date. The band pass and radiance specifications are from *Markham and Barker* [1985, 1987], while saturation reflectances are calculated from their data.

sured from normal to the surface), and $L(\mu, \phi)$ is the upward spectral radiance at the angle arccos μ and azimuth ϕ.

Apparent planetary reflectance, R_p, is the apparent spectral albedo of the Earth and atmosphere if the reflected radiation is assumed to have an isotropic distribution [*Nicodemus et al.*, 1977]:

$$R_p(\lambda) = \frac{\pi d^2 L(\lambda)}{\mu_0 S_0(\lambda)} \quad (2)$$

where d is the Earth-Sun distance in astronomical units, $L(\lambda)$ is the satellite measured radiance in spectral band λ, and $S_0(\lambda)$ is the exoatmospheric solar irradiance in band λ.

Snow water equivalence (SWE) is the product of snow pack depth and density. It is often expressed as the depth of liquid water equivalence, 1 kg m^{-2} = 1 mm.

A.2. Spectral Signatures of Snow and Other Surface Materials in the TM Band Passes

Table A1 summarizes the TM's reflective band passes. The recorded radiance in each band is quantized as an 8-bit digital

radiance number (DN) from 0 to 255. The quantization step differs for each band because of detector design and because solar irradiance varies across the spectrum.

Figure A1 displays calculated reflectance spectra for deep, pure snow in the TM band passes. Pure snow is a distinctive target in the TM's reflective bands, being among the brightest of natural substances in the visible and near infrared part of the spectrum (VNIR, bands 1–4) but among the darkest in the shortwave infrared (SWIR, bands 5 and 7). The spectral variability of the albedo of snow is controlled by the absorption coefficient of ice, k, the imaginary part of the refractive index. Absorption in ice reaches a minimum at wavelength 0.46 μm, but increases by 10^7 as wavelength increases out to 2.5 μm [*Warren*, 1982]. The e-folding distance for ice, the distance over which transmittance is reduced to e^{-1}, decreases from 22.5 m at the center wavelength of TM band 1 to only 679 μm at the center of band 5 (Table A2).

Light in snow is scattered primarily by refraction through, not reflection from, the ice grains. Photons are scattered at the grain surfaces, but absorbed while traversing the grain interiors. *Bohren and Barkstrom* [1974] found that only about 3% of the light scattered by an ice grain is reflected from the external surface, while nearly 89% is refracted through the grain and 8% is scattered after internal reflections. Because ice is so
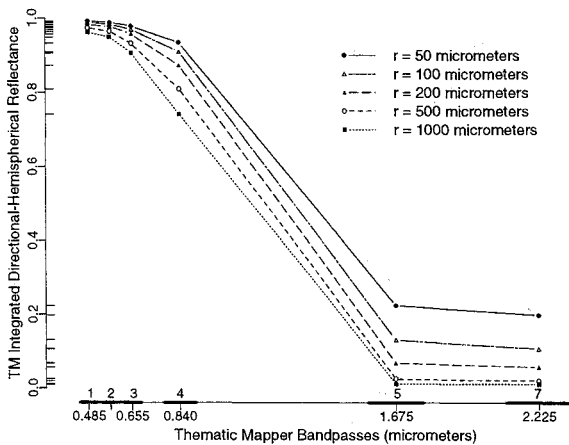
Figure A1. Directional-hemispherical reflectance of deep, pure snow in the TM band passes. Reflectance in the visible bands is insensitive to ice grain size, while reflectance in the SWIR bands is sensitive for the smallest grains. Displayed values are calculated for snow of semi-infinite optical depth using a two-stream approximation to the radiative transfer equation [*Dozier and Marks*, 1987].

Table A2. Light Absorption by Ice

Band	Band Pass Center, μm	k	e-Folding Distance
1	0.485	1.709×10^{-9}	22.6 m
2	0.570	3.520×10^{-9}	12.9 m
3	0.655	1.543×10^{-8}	3.38 m
4	0.840	1.510×10^{-7}	426 mm
5	1.675	1.964×10^{-4}	679 μm
7	2.225	2.143×10^{-4}	826 μm

Light absorption by ice in the Landsat-5 Thematic Mapper band passes. The absorption coefficient of ice, k, is the imaginary part of the complex refractive index. The e-folding distance is the distance through ice over which the transmittance is reduced to e^{-1}. Values given are for the band pass centers. This table demonstrates why grain size has little influence on visible reflectance but becomes important at longer wavelengths.

transparent to visible radiation, snow reflectance is insensitive to grain size in TM bands 1, 2, and 3. However, reflectance in these bands is sensitive to absorbing impurities in the snow (mainly dust and soot) and to SWE, because the ground can absorb light that penetrates optically thin snow packs [*Wiscombe and Warren*, 1980; *Warren and Wiscombe*, 1980]. Absorption by ice is much stronger in bands 5 and 7, so reflectance at these wavelengths is insensitive to absorbing impurities and SWE, but sensitive to grain size. Absorbing particulates affect snow reflectance out to 0.9 μm [*Grenfell et al.*, 1981], so band 4 is sensitive to moderate amounts of impurities and also sensitive to grain size.

The spectral signatures of other common scene constituents differ markedly from that of snow. Clouds and snow are both bright to the TM's VNIR detectors (bands 1–4), but clouds are much brighter than snow in the SWIR region (bands 5 and 7) because the smaller sizes of the scatterers in clouds decrease the probability of absorption in this spectral region where ice and water are moderately absorptive [*Crane and Anderson*, 1984; *Dozier*, 1984, 1989]. Conversely, bodies of open water are dark at all wavelengths. Vegetation is dark in the visible bands because of absorption by photosynthetic pigments, but has a reflectance peak in band 4 because of leaf cell structure [*Hoffer*, 1978]. Reflectance in bands 5 and 7 is inversely related to leaf water content for healthy vegetation, and is high compared to that of snow. Most rocks and soils present spectra that are the inverse of snow's, with absorption by iron oxides and organic matter producing reflectances that are low in the visible bands but high in the SWIR.

A.3. Spectral Mixture Analysis

The measured pixel reflectance in band b using N image or reference library end members is modeled as

$$R_b = \varepsilon_b + \sum_{n=1}^{N} r_{bn} f_n \qquad (3)$$

R_b is the measured reflectance in band b (from the satellite image), ε_b is the error between the model and the measurement in band b, r_{bn} is the reflectance in band b from end member n (chosen from the image or a library of reference reflectance spectra), and f_n is the fraction of the pixel occupied by end member n. Common model constraints are that the end member fractions either sum to 1 or be nonnegative and sum to not more than 1. The goodness-of-fit of the model is measured by the average root-mean-square error ($\overline{\mathrm{RMSE}}$) in all bands for all pixels in the modeled region.

First used to identify components in chemical mixtures [*Lawton and Sylvestre*, 1971], mixture modeling has been used as a remote sensing tool to identify minerals on the lunar and Martian surfaces [*Johnson et al.*, 1985; *Adams et al.*, 1986], map regional vegetation and geologic substrates [*Smith et al.*, 1990], estimate vegetation canopy densities [*Ustin et al.*, 1988], and estimate fluvial suspended sediment concentrations, a nonlinear mixing problem [*Mertes et al.*, 1993]. *Smith et al.* [1990] showed that in Owens Valley the linear mixing assumption is valid for the waxy, semiopaque foliage of arid environments despite wide variation in soil brightness, and that the best set of reference end members does not change with seasonal illumination and canopy density.

Spectral mixture analysis can normalize for different topographic illumination if the spectra maintain characteristic shapes that differ primarily in amplitude across the full range of scene illumination. If the fractions of the materials within a pixel are constrained to be nonnegative and to sum to not more than 1, then the sum of those fractions is proportional to the illumination on the pixel. If one fraction is ratioed against the sum, the result is the fraction of the pixel occupied by that material if the pixel spectrum is a linear combination of the contributing spectra and if the contributing spectra are well chosen, that is, they are good representatives of the spectra of the materials in the pixel.

If materials are spatially segregated within a pixel and incident photons interact with only one surface material, then the spectral mixture is macroscopic and can be modeled as a linear combination of the pure component spectra. Intimate mixtures occur if surface materials are distributed so that photons interact with multiple components; the component spectra may then combine nonlinearly.

Possible sources of nonlinear mixing in snow are VNIR absorption by contaminating particulates or by the substrate, SWIR absorption by ice (which increases with particle size), anisotropic reflectance (snow is a forward scattering medium), topographic illumination, and light scattered upward from the snow pack through the forest canopy. We evaluated each of these and found that the linear mixing assumption is appropriate for mapping montane snow packs at subpixel resolution [*Rosenthal*, 1993].

A.4. Decision Tree Methods

The data used to grow a decision tree are arrayed in a learning sample $\mathcal{L}$. Each case in $\mathcal{L}$ contains a set of predictor variables (in this study, TM band values from a randomly drawn set of pixels) and a response variable (the corresponding estimated scaled snow fraction from the spectral mixture analysis). The entire sample (or root node) is then partitioned into the two more homogeneous subsets (descendant nodes) that most reduce the "impurity" of the set of responses in $\mathcal{L}$. The data are typically split on the value of a single predictor variable, though splits on linear and boolean combinations of variables are possible.

The process is recursively repeated on each descendant node. When either the inhomogeneity or number of cases at a node falls below a specified level, the splitting is stopped, and the node is considered terminal. In principle, the splitting can be continued until all descendant subsets contain only identical response variables, but such a tree would overfit the data and have an optimistic misclassification rate of 0.

Sonquist and Morgan [1964] introduced tree-structured multivariate regression. A node was split into the two subgroups that produced the largest reduction in the unexplained sum of squares. The χ-squared statistic [*Kass*, 1980] and the likelihood function [*Ciampi et al.*, 1987; *Clark and Pregibon*, 1992] have also been used as the bases for splits and for merging similar terminal nodes. *Breiman et al.* [1984] eliminated the need for a stopping rule by growing an oversized tree and then pruning it back by minimizing a cost complexity measure: the sum of the tree misclassification rate and a penalty for the size of the tree.

Decision trees offer several advantages over other techniques of data analysis. Error estimates are provided as a direct consequence of the splitting procedure; the classification tree error rate is the ratio of misclassified cases to the total number of cases, while the standard error of regression tree estimates is the square root of the mean residual deviance for all terminal nodes. The splitting criteria are easier to understand from

physical principles than the equations produced by multiple linear regression or the hidden node weights of neural networks. Decision trees are robust to outliers and misclassified input, which tend to be segregated into small terminal nodes.

The decision trees developed here use the likelihood function in splitting and pruning algorithms for classification trees, and the reduction of the residual sum of squares as the splitting criterion for regression trees [*Becker et al.*, 1988; *Clark and Pregibon*, 1992]. The goodness-of-split criterion is the reduction in deviance from a parent node to its descendants. For regression trees the deviance D of response variable y within a node with mean μ is

$$D = (y - \mu)^2 \qquad (4)$$

and the deviance for the entire node is the residual sum of squares. For classification trees the deviance of response variable y is

$$D = -2 \sum_{k=1}^{K} y_{ik} \log (p_{ik}) \qquad (5)$$

where K is the number of classes, p_{ik} is the probability of case i falling into class k, and y_{ik} is 1 if y_i falls into class k, and 0 otherwise. If a node is pure (i.e., contains only identical observations) then $D = 0$. The deviance of a node is the sum of the deviances of the observations contained within it. The split chosen at a node is the one that produces the greatest reduction in deviance by maximizing $D_{\text{parent}} - (D_{\text{left}} + D_{\text{right}})$.

References

Adams, J. B., M. O. Smith, and P. E. Johnson, Spectral mixture modeling: a new analysis of rock and soil types at the Viking Lander 1 site, *J. Geophys. Res.*, *91*(B8), 8098–8112, 1986.

Baumgartner, M. F., K. Seidel, and J. Martinec, Large area snowmelt runoff simulations based on Landsat-MSS data, *Proc. IGARSS '85*, *1*, 30–38, 1985.

Becker, R. A., J. M. Chambers, and A. R. Wilks, *The New S Language: A Programming Environment for Data Analysis and Graphics*, Wadsworth and Brooks/Cole Advanced Books and Software, Pacific Grove, CA, 1988.

Boardman, J. W., Inversion of imaging spectrometry data using singular value decomposition, *Proc. IGARSS '89*, *4*, 2069–2072, 1989.

Bohren, C. F., and B. R. Barkstrom, Theory of the optical properties of snow, *J. Geophys. Res.*, *79*, 4527–4535, 1974.

Breiman, L., J. H. Friedman, R. A. Olshen, and C. J. Stone, *Classification and Regression Trees*, Wadsworth, Belmont, Calif., 1984.

Ciampi, A., C.-H. Chang, S. Hogg, and S. McKinney, Recursive partition: A versatile method for exploratory data analysis in biostatistics, in *Biostatistics*, edited by I. B. MacNeill and G. J. Umphrey, pp. 23–50, D. Reidel, Norwell, Mass., 1987.

Clark, L. A., and D. Pregibon, Tree-based models, in *Statistical Models in S*, edited by J. M. Chambers and T. J. Hastie, pp. 377–419, Wadsworth and Brooks/Cole Advanced Books and Software, Pacific Grove, CA, 1992.

Crane, R. G., and M. R. Anderson, Satellite discrimination of snow/cloud surfaces, *Int. J. Remote Sens.*, *5*(1), 213–223, 1984.

Crippen, R. E., The regression intersection method of adjusting image data for band ratioing, *Int. J. Remote Sens.*, *8*(2), 137–155, 1987.

Crippen, R. E., The dangers of underestimating the importance of data adjustments in band ratioing, *Int. J. Remote Sens.*, *9*(4), 767–776, 1988.

Dozier, J., Snow reflectance from Landsat-4 Thematic Mapper, *IEEE Trans. Geosci. Remote Sens.*, *22*(3), 323–328, 1984.

Dozier, J., Spectral signature of alpine snow cover from the Landsat Thematic Mapper, *Remote Sens. Environ.*, *28*, 9–22, 1989.

Dozier, J., and J. Frew, Rapid calculation of terrain parameters for radiation modeling from digital elevation data, *IEEE Trans. Geosci. Remote Sens.*, *28*(5), 963–969, 1990.

Dozier, J., and D. Marks, Snow mapping and classification from Landsat Thematic Mapper data, *Ann. Glaciol.*, *9*, 97–103, 1987.

Gleick, P. H., Regional hydrologic consequences of increases in atmospheric CO_2 and other trace gases, *Clim. Change*, *10*, 137–161, 1987.

Grenfell, T. C., D. K. Perovich, and J. A. Ogren, Spectral albedos of an alpine snowpack, *Cold Regions Sci. Technol.*, *4*, 121–127, 1981.

Hoffer, R. M., Biological and physical considerations in applying computer-aided analysis techniques to remote sensor data, in *Remote Sensing: The Quantitative Approach*, edited by P. H. Swain and S. M. Davis, McGraw-Hill, New York, 1978.

Johnson, P. E., M. O. Smith, and J. B. Adams, Quantitative analysis of planetary reflectance spectra with principal components analysis, *J. Geophys. Res.*, *90*, c805–c810, 1985.

Kahrl, W. T., (Ed.), *The California Water Atlas*, Governor's Off. of Plann. and Res., Sacramento, Calif., 1978.

Kass, G. V., An exploratory technique for investigating large quantities of categorical data, *Appl. Stat.*, *29*(2), 119–127, 1980.

Lawton, W. H., and E. A. Sylvestre, Self modeling curve resolution, *Technometrics*, *13*(3), 617–633, 1971.

Markham, B. L., and J. L. Barker, Spectral characterization of the Landsat Thematic Mapper sensors, *Int. J. Remote Sens.*, *6*(5), 697–716, 1985.

Markham, B. L., and J. L. Barker, Thematic Mapper bandpass solar exoatmospheric irradiances, *Int. J. Remote Sens.*, *8*(3), 517–523, 1987.

Martinec, J., and A. Rango, Areal distribution of snow water equivalent evaluated by snow cover monitoring, *Water Resour. Res.*, *17*(5), 1480–1488, 1981.

Meador, W. E., and W. R. Weaver, Two-stream approximations to radiative transfer in planetary atmospheres: A unified description of existing methods and a new improvement, *J. Atmos. Sci.*, *37*, 630–643, 1980.

Mertes, L. A. K., M. O. Smith, and J. B. Adams, Estimating suspended sediment concentrations in surface waters of the Amazon River wetlands from Landsat images, *Remote Sens. Environ.*, *43*, 281–301, 1993.

Nicodemus, F. E., J. C. Richmond, J. J. Hsia, I. W. Ginsberg, and T. Limperis, Geometrical considerations and nomenclature for reflectance, *Monogr. 160*, Natl. Bur. of Stand., Washington, D. C., 1977.

Rango, A., and K. I. Itten, Satellite potentials in snowcover monitoring and runoff prediction, *Nordic Hydrol.*, *7*, 209–230, 1976.

Rango, A., and J. Martinec, Application of a snowmelt-runoff model using Landsat data, *Nordic Hydrol.*, *10*, 225–238, 1979.

Richards, J. A., *Remote Sensing Digital Image Analysis: An Introduction*, 2nd ed., Springer-Verlag, New York, 1993.

Rosenthal, C. W., Mapping montane snow cover at subpixel resolution from the Landsat Thematic Mapper, M.A. thesis, Univ. of Calif., Santa Barbara, 1993.

Running, S. W., et al., Terrestrial remote sensing science and algorithms planned for EOS/MODIS, *Int. J. Remote Sens.*, *15*(17), 3587–3620, 1994.

Satterwhite, M. B., and J. P. Henley, Hyperspectral signatures (400 to 2500 nm) of vegetation, minerals, soils, rocks, and cultural features: Laboratory and field measurements, *Tech. Rep. ETL-0573*, U.S. Army Corps of Eng., Eng. Topogr. Lab., Fort Belvoir, Va., 1990.

Smith, M. O., S. L. Ustin, J. B. Adams, and A. R. Gillespie, Vegetation in deserts, 1, A regional measure of abundance from multispectral images, *Remote Sens. Environ.*, *29*, 1–26, 1990.

Sonquist, J. A., and J. N. Morgan, The detection of interaction effects, *Monog. 35*, Surv. Res. Cent., Inst. for Soc. Res., Univ. of Mich., Ann Arbor, 1964.

Storer, T. I., and R. L. Usinger, *Sierra Nevada Natural History*, Univ. of Calif. Press, Berkeley, 1962.

Ustin, S. L., M. O. Smith, and J. B. Adams, Vegetation patterns derived from Landsat Thematic Mapper images in Owens Valley, in *Plant Biology of Eastern California*, edited by C. A. Hall Jr. and V.

Doyle-Jones, pp. 293–302, White Mount. Res. Stn., Univ. of Calif., Los Angeles, 1988.

Warren, S. G., Optical properties of snow, *Rev. Geophys.*, *20*(1), 67–89, 1982.

Warren, S. G., and W. J. Wiscombe, A model for the spectral albedo of snow, 2, Snow containing atmospheric aerosols, *J. Atmos. Sci.*, *37*(12), 2734–2745, 1980.

Weeden, N. F., *A Sierra Nevada Flora*, Wilderness Press, Berkeley, Calif., 1981.

Whitney, S., *Western Forests*, Audubon Society Nature Guides, Knopf, New York, 1985.

Wiscombe, W. J., and S. G. Warren, A model for the spectral albedo of snow, 1, Pure snow, *J. Atmos. Sci.*, *37*(12), 2712–2733, 1980.

J. Dozier, School of Environmental Science and Management, University of California, 4670 Physical Sciences North, Santa Barbara, CA 93106. (e-mail: dozier@esm.ucsb.edu)

W. Rosenthal, Institute for Computational Earth System Science, University of California, Santa Barbara, CA 93106. (e-mail: walter@icess.ucsb.edu)